AGU PUBLICATIONS

JGR

Journal of Geophysical Research: Solid Earth

RESEARCH ARTICLE
10.1002/2017JB014636

Special Section:
Seismic and micro-seismic signature of fluids in rocks: Bridging the scale gap

Modeling Forced Imbibition Processes and the Associated Seismic Attenuation in Heterogeneous Porous Rocks

Santiago G. Solazzi[1], Luis Guarracino[1], J. Germán Rubino[2], Tobias M. Müller[3], and Klaus Holliger[4]

[1]CONICET, Facultad de Ciencias Astronómicas y Geofísicas, Universidad Nacional de La Plata, La Plata, Argentina, [2]CONICET, Centro Atómico Bariloche-CNEA, San Carlos de Bariloche, Argentina, [3]Commonwealth Scientific and Industrial Research Organization, Energy, Perth, Western Australia, Australia, [4]Applied and Environmental Geophysics Group, Institute of Earth Sciences, University of Lausanne, Lausanne, Switzerland

Key Points:
- We perform numerical simulations of imbibition in a rock sample and compute seismic attenuation through a numerical upscaling procedure
- Our results show that two attenuation peaks, associated with the saturation front and isolated fluid patches, can arise
- The injection rate of the imbibition process controls the amplitude of the two attenuation peaks

Correspondence to:
S. G. Solazzi,
ssolazzi@fcaglp.unlp.edu.ar

Citation:
Solazzi, S. G., Guarracino, L., Rubino, J. G., Müller, T. M., & Holliger, K. (2017). Modeling forced imbibition processes and the associated seismic attenuation in heterogeneous porous rocks. *Journal of Geophysical Research: Solid Earth*, *122*. https://doi.org/10.1002/2017JB014636

Received 29 JUN 2017
Accepted 3 OCT 2017
Accepted article online 9 OCT 2017

Abstract Quantifying seismic attenuation during laboratory imbibition experiments can provide useful information toward the use of seismic waves for monitoring injection and extraction of fluids in the Earth's crust. However, a deeper understanding of the physical causes producing the observed attenuation is needed for this purpose. In this work, we analyze seismic attenuation due to mesoscopic wave-induced fluid flow (WIFF) produced by realistic fluid distributions representative of imbibition experiments. To do so, we first perform two-phase flow simulations in a heterogeneous rock sample to emulate a forced imbibition experiment. We then select a subsample of the considered rock containing the resulting time-dependent saturation fields and apply a numerical upscaling procedure to compute the associated seismic attenuation. By exploring both saturation distributions and seismic attenuation, we observe that two manifestations of WIFF arise during imbibition experiments: the first one is produced by the compressibility contrast associated with the saturation front, whereas the second one is due to the presence of patches containing very high amounts of water that are located behind the saturation front. We demonstrate that while the former process is expected to play a significant role in the case of high injection rates, which are associated with viscous-dominated imbibition processes, the latter becomes predominant during capillary-dominated processes, that is, for relatively low injection rates. We conclude that this kind of joint numerical analysis constitutes a useful tool for improving our understanding of the physical mechanisms producing seismic attenuation during laboratory imbibition experiments.

1. Introduction

Immiscible two-phase flow processes in porous media are very common in the Earth's crust. Notably, they play a prominent role during the injection and extraction of fluids, as a result of which complex distributions of patches of the associated fluid phases tend to be formed (e.g., Alemu et al., 2013). The spatial distribution and, in particular, the geometrical details of these patches are controlled by the physical properties of the fluid phases and rock matrix, the geometrical characteristics of the heterogeneities present in the geological formation, the initial fluid distribution, and the fluid injection or extraction rates. Knowledge regarding the temporal evolution of the pore fluid distribution is of significant importance in many fields of Earth engineering and environmental sciences, including groundwater management and remediation, characterization of gas hydrate reservoirs, enhanced oil and gas recovery, and monitoring of CO_2 sequestration in brine-saturated formations.

If, during fluid injection/extraction operations, one pore fluid phase is replaced by another one having a different compressibility, the effective stiffness of the material changes and so does the velocity of compressional seismic waves propagating through the medium. Moreover, in the presence of mesoscopic heterogeneities associated with the fluid distributions, that is, regions predominantly saturated with one fluid phase and having sizes larger than the typical pore diameter but smaller than the prevailing seismic wavelengths, seismic waves can experience significant attenuation and velocity dispersion due to mesoscopic wave-induced fluid flow (WIFF) (e.g., Müller et al., 2010). This implies that seismic data contain information not only about the

presence of different fluid phases but also on the geometrical characteristics of the fluid saturation patterns. For these reasons, seismic methods are becoming increasingly important for monitoring injection or extraction of fluids in the Earth's crust. However, to retrieve this kind of information from seismic data, we need a profound knowledge on the characteristics of fluid distributions expected to arise during such operations as well as on the physical processes governing the propagation of seismic waves in such environments.

Laboratory experiments provide unique opportunities for broadening the current understanding of multiphase flow, the resulting fluid distribution patterns, and their impact on seismic signatures. In particular, imbibition processes, where an injected wetting fluid phase displaces an already present nonwetting phase from the rock pores, can provide valuable information in this regard. These kinds of experiments generate pore fluid distribution patterns determined by the host rock heterogeneity through the combined effects of capillary, gravity, and viscous forces (e.g., Shi et al., 2011). Experimental evidence indicates that the resulting heterogeneous saturation patterns can produce significant seismic attenuation (e.g., Tisato & Quintal, 2013). One of the key parameters involved in imbibition experiments is the fluid injection rate. Indeed, laboratory imbibition experiments performed on pore-scale networks indicate that high injection rates lead to viscous-dominated stable fluid displacements, characterized by a piston-like advance, whereas low injection rates lead to capillary-dominated discontinuous displacements, characterized by a disconnected advance (e.g., Lenormand, 1990; Lenormand & Zarcone, 1984). Also, changing the injection rate has significant effects on the seismic response, as recently observed in laboratory experiments (Lopes & Lebedev, 2012; Lopes et al., 2014). However, the details of the physical causes of the seismic attenuation observed during imbibition processes and, in particular, its relation with the injection rate remain enigmatic.

The quantitative interpretation of the physical mechanisms contributing to the seismic attenuation observed during imbibition experiments is not a simple task. A key aspect of the WIFF attenuation mechanism is that it scales with the compressibility contrasts between the different mesoscopic regions (e.g., Müller et al., 2010). In the case of partially saturated porous media, attenuation levels are expected to be significant if the pore fluids have contrasting compressibilities, such as those employed in typical imbibition experiments. Indeed, WIFF is currently considered to be a predominant seismic attenuation mechanism arising during imbibition experiments (e.g., Tisato & Quintal, 2013; Yin et al., 1992). Corresponding interpretation efforts performed in the framework of WIFF can be based on analytical models (e.g., Pride et al., 2004; White, 1975) or numerical upscaling procedures (e.g., Masson & Pride, 2007; Rubino et al., 2009). However, these approaches are either inherently limited or have so far only been used with very simple fluid distributions. For instance, some analytical models are restricted to porous rocks containing binary patches of two types of fluids (e.g., Johnson, 2001; Pride et al., 2004; White, 1975). Numerical upscaling approaches are more flexible in this regard, but, so far, most related works only considered binary patchy saturation patterns based on stochastic processes (e.g., Masson & Pride, 2011; Rubino et al., 2011). However, there are physical reasons that render the existence of binary gas-water distributions unlikely. In fact, laboratory studies show that core samples subjected to injection processes involving immiscible fluids evidence spatially continuous patchy saturation patterns (e.g., Cadoret et al., 1995; Toms-Stewart et al., 2009). As far as the authors know, very little work has so far been done with regard to the interpretation of seismic signatures of partially saturated rocks in the presence of realistic saturation patterns in general and in the case of imbibition processes in particular. Qi et al. (2014) modeled seismic attenuation using a continuous random media (CRM) model of patchy saturation including capillary effects. The information required by the CRM model was derived from binarized X-ray images of the pore fluid distribution during a laboratory imbibition test. Recently, Liu et al. (2016) incorporated patch size variability into the CRM model. Particularly, they proposed a model to explain the experimental results of Lopes and Lebedev (2012) and Lopes et al. (2014), where ultrasonic velocities were measured during imbibition experiments performed with variable injection rates. Their results suggest that a relation may exist between injection rate and patch size. Kuteynikova et al. (2014) modeled WIFF in homogenous rock samples saturated with continuous air-water distributions. They observed that even relatively small variations in the spatial distribution of the pore fluids can significantly change the attenuation values. Rubino and Holliger (2012) explored seismic attenuation in heterogeneous rocks containing spatially continuous gas-water saturation fields. However, these authors linked the rock frame heterogeneities to the saturation of the fluid phases by assuming that the rock sample was in capillary pressure equilibrium, a condition that is not satisfied during imbibition experiments. Imbibition processes evidence time-dependent saturation distributions that can be modeled by solving the two-phase flow equations under adequate initial and boundary conditions.

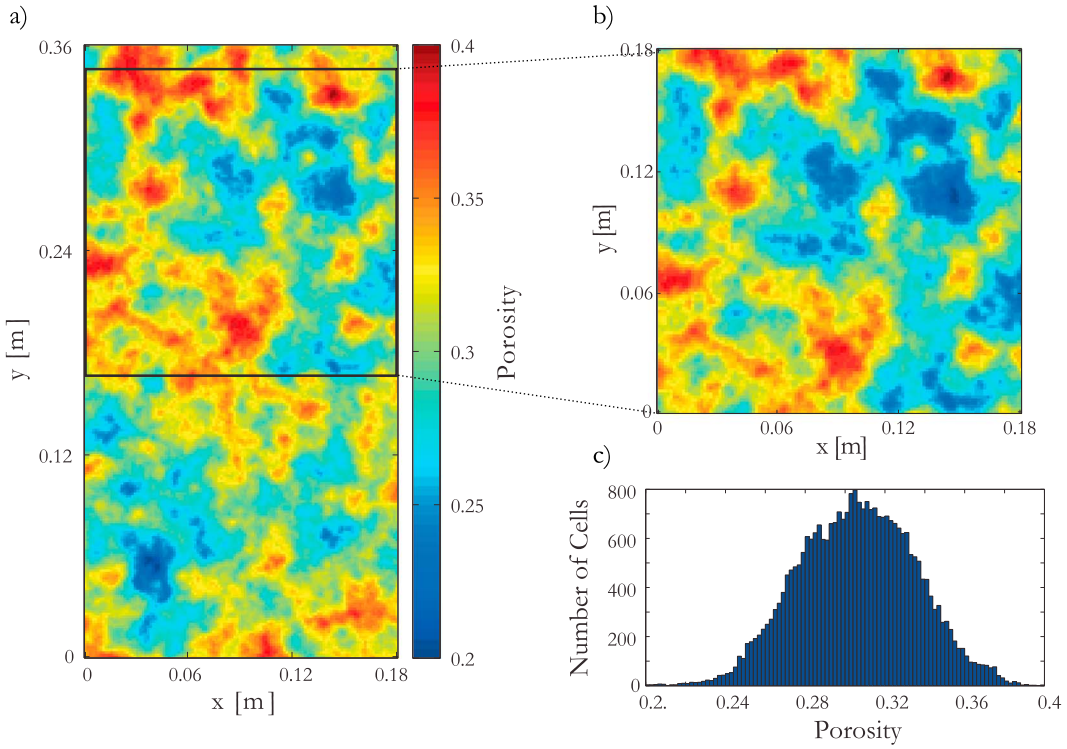

Figure 1. (a) Two-dimensional heterogeneous porosity field considered in the numerical imbibition tests and (b) subsample considered to analyze seismic attenuation. (c) Histogram of the porosity of the subsample characterized by a mean of 0.3 and a standard deviation of 0.029.

A joint analysis considering two-phase flow processes and the quantification of the associated seismic attenuation due to WIFF is therefore needed to shed light onto the importance of this energy dissipation mechanism.

In this work, we analyze the characteristics of the saturation fields that arise during imbibition experiments and their impact on seismic signatures. To do so, we first perform numerical simulations of imbibition processes in a heterogeneous sandstone sample by solving the 2-D two-phase flow equations using an implicit pressure-explicit saturation approach. We then select a subsample of the considered rock frame, containing the time-dependent saturation fields obtained from the flow simulations, and apply a numerical upscaling procedure that allows to quantify the associated seismic attenuation in response to WIFF. A comprehensive numerical analysis is performed to explore the importance of this seismic attenuation mechanism during imbibition experiments, its temporal evolution, and the role played by the injection rate.

2. Numerical Models and Theoretical Background

2.1. Heterogeneous Rock Sample and Physical Properties

To explore the geometrical characteristics of partial gas-water distributions during imbibition processes and their impact on the resulting attenuation of seismic waves, we consider a rectangular 2-D synthetic rock sample with a height of 36 cm and a width of 18 cm. The sample represents a heterogeneous sandstone containing spatially continuous variations of the dry frame properties, which are parameterized as functions of porosity (Figure 1a). Following Tronicke and Holliger (2005), the porosity field is obtained using a stochastic procedure based on a von Karman-type spectral density function. We consider a stochastic process with a spatially isotropic correlation length of 1.05 cm. While the sample shown in Figure 1a is employed to perform numerical imbibition experiments, the associated seismic signatures are computed for a square subsample of 18 cm side length (Figure 1b), whose porosity distribution has a mean value of 0.3 and a standard deviation of 0.029. Figure 1c shows the corresponding histogram. We assume that the rock frame is composed of quartz grains with the physical properties given in Table 1.

Variations in porosity imply changes in other physical properties of the rock sample, including permeability, entry pressure, and frame elastic moduli. We use the Kozeny-Carman equation to relate the porosity value

Table 1
Material Properties for the Models Considered in This Study

Material	Properties		
Solid phase	Bulk Modulus	Shear Modulus	
Quartz	$K_s = 37$ GPa	$\mu_s = 44$ GPa	
Fluid phases	Bulk Modulus	Viscosity	Density
Water	$K_w = 2.3$ GPa	$\eta_w = 0.001$ Pa s	$\rho_w = 1.09$ g/cm^3
Gas	$K_g = 0.012$ GPa	$\eta_g = 0.00015$ Pa s	$\rho_g = 0.078$ g/cm^3

Note. Adopted from Rubino and Holliger (2012) and Rubino et al. (2011).

ϕ of the rock sample to the permeability κ (Carman, 1937; Kozeny, 1927). This relation can be expressed as (Mavko et al., 2009)

$$\kappa(\phi) = B\frac{\phi^3}{(1-\phi)^2}d_s^2, \tag{1}$$

where $B = 1/72\tau^2$ is a geometric factor that depends on the tortuosity τ of the porous sample and d_s denotes the mean diameter of the solid grains. For the numerical simulations considered in our work, we assume $d_s = 130$ μm, which constitutes a representative value for quartz-grained sandstones (e.g., Renaud et al., 2013). Also, we take $\tau = 3.45$, in agreement with the approximate tortuosity of Fontainebleau sandstone (Mair et al., 1999), which is widely regarded as a representative example of a clean quartz sandstone.

The entry pressure p_d, which is the capillary pressure value at full saturation, partly determines the capillary behavior of imbibition processes. In fact, the entry pressure is conditioned by the porosity structure (e.g., Bear, 1972). We use Leverett scaling to determine the entry pressure values (Leverett, 1941)

$$p_d(\phi) = \gamma\sqrt{\frac{\phi}{\kappa(\phi)}}, \tag{2}$$

where γ is the interfacial tension between gas and water. This parameter is taken as $\gamma \simeq 65 \times 10^{-3}$ N/m, in accordance with the values reported for methane-water interfaces at 10 MPa (Ren et al., 2000).

Finally, to link the porosity ϕ with the bulk and shear moduli of the dry rock, we use the model proposed by Pride (2005)

$$K_m = K_s\frac{(1-\phi)}{(1+c_s\phi)}, \tag{3}$$

$$\mu_m = \mu_s\frac{(1-\phi)}{(1+1.5c_s\phi)}, \tag{4}$$

where μ_m is the undrained shear modulus of the material, which is equal to that of the dry frame, and K_m is the bulk modulus of the dry matrix. K_s and μ_s denote the bulk and shear moduli of the quartz solid grains, respectively. Corresponding values are given in Table 1. The degree of consolidation between the grains is given by the so-called consolidation parameter c_s. In the case of consolidated sandstones, c_s ranges from 2 to 20 (Pride, 2005). Following the work of Pride and Berryman (2003), we take $c_s = 10$.

2.2. Two-Phase Immiscible Flow Equations and Imbibition Processes

In the following, we model a forced imbibition process where water is injected at a constant rate into a heterogeneous porous rock sample mostly saturated with gas. The mathematical model of two-phase flow in porous media is commonly based on the assumption that each fluid phase is governed by mass conservation equation and Darcy's law (e.g., Bear, 1972). We consider water as a wetting phase and gas as a nonwetting phase, indexed by w and g, respectively. The mass balance equation and Darcy's law for the two immiscible fluid phases are given by

$$\frac{\partial\left(\phi\rho_\beta S_\beta\right)}{\partial t} + \nabla\cdot\left(\rho_\beta \mathbf{q}_\beta\right) = 0, \tag{5}$$

$$\mathbf{q}_\beta = -\frac{\kappa\, k_{r,\beta}}{\eta_\beta}\left(\nabla p_\beta - \rho_\beta \mathbf{g}\right), \tag{6}$$

where $\beta \in \{w, g\}$, t denotes the time, and $\mathbf{g}$ the gravitational acceleration vector. The symbols ρ_β, S_β, $\mathbf{q}_\beta$, η_β, $k_{r,\beta}$, and p_β stand for the density, saturation, Darcy velocity, dynamic viscosity, relative permeability, and pressure of phase β, respectively. The saturations of the two fluid phases are constrained by

$$S_w + S_g = 1, \tag{7}$$

whereas their pressures are related by the capillary pressure

$$p_c = p_g - p_w. \tag{8}$$

The above mentioned equations need to be complemented with constitutive relations that effectively capture the complexities of pore-scale processes. In this case, equations (5)–(8) are solved together with two nonlinear constitutive models that quantify the relative permeability and the capillary pressure as functions of water saturation.

Capillary pressure is assumed to obey the nonhysteric Brooks and Corey (1964) relation

$$p_c\left(S_{\mathrm{we}}\right) = p_d S_{\mathrm{we}}^{-\frac{1}{\lambda}}, \tag{9}$$

where λ is a parameter that characterizes the pore size distribution. In the case of consolidated sandstones, the capillary behavior has been successfully described with λ values ranging from 1.4 to 2.7 (Pini & Benson, 2017). For the numerical simulations considered in this work, we therefore employ $\lambda = 2$. The effective saturation of the wetting fluid is given by $S_{\mathrm{we}} = (S_w - S_{\mathrm{wr}})/(1 - S_{\mathrm{wr}})$, where S_{wr} is the irreducible water saturation. We take $S_{\mathrm{wr}} = 5\%$, in accordance with the approximate irreducible water saturation of Fontainebleau sandstone (Mavko et al., 2009).

The relative permeability-saturation relationships can be obtained using equation (9) in the predictive model of Burdine (1953)

$$k_{r,w}\left(S_{\mathrm{we}}\right) = S_{\mathrm{we}}^{3+\frac{2}{\lambda}}, \tag{10}$$

$$k_{r,g}\left(S_{\mathrm{we}}\right) = \left(1 - S_{\mathrm{we}}\right)^2 \left(1 - S_{\mathrm{we}}^{1+\frac{2}{\lambda}}\right). \tag{11}$$

The aforementioned two-phase flow equations are subjected to appropriate initial and boundary conditions to describe the initial state and injection rates that mimic laboratory experiments. As we intend to emulate a forced imbibition process, we impose a constant Darcy velocity for the water phase along the top boundary $-q_w^T$, whereas that corresponding to the gas phase is forced to be null. The left and right boundaries of the sample are sealed; that is, we impose no-flow boundary conditions. A constant pressure for the wetting phase and a constant saturation are defined along the bottom of the sample. More detailed information with regard to the initial and boundary conditions employed in the flow simulations is provided in Appendix A.

The system of equations (5)–(11), together with the selected initial and boundary conditions, is solved by means of an implicit pressure-explicit saturation approach. The pressure equation and the saturation equation are solved sequentially by means of a hybridized mixed finite element method combined with a discontinuous Galerkin approach (Hoteit & Firoozabadi, 2008). We use a zero-order Raviart-Thomas space (Raviart & Thomas, 1977) to represent the Darcy velocities and a first-order polynomial approximation to represent the wetting phase saturation. An explicit forward Euler method is employed for the time discretization of the partial differential equations arising from equation (5). The time step is selected adaptatively satisfying the Courant-Friderichs-Lewy condition (Courant et al., 1928), that is, using a criterion that ensures the stability of the saturation equation.

It is important to remark here that although we perform the flow simulations in a rectangular sample, shown in Figure 1a, we choose a subsample of the domain far enough from the bottom boundary (Figure 1b) to analyze the associated seismic signatures. This allows for studying the characteristics of seismic attenuation in a region where saturation patterns are not influenced by the constant saturation condition imposed along the bottom boundary.

2.3. Numerical Upscaling Procedure for Quantifying WIFF Effects

When a seismic wave propagates through a fluid-saturated porous rock that contains mesoscopic heterogeneities with contrasting compressibilities, pore fluid pressure gradients arise due to the stresses associated with the passing wavefield. These pressure gradients induce fluid flow and energy dissipation through internal friction, which manifests itself in the form of seismic attenuation.

In order to quantify the WIFF effects produced by the heterogeneous saturation patterns resulting from the previously described numerical imbibition experiments, we choose a subsample (Figure 1b) of the original rock sample where the flow equations were solved. We then saturate the subsample with the fluid distributions obtained from the flow simulations for a certain instant of interest and apply the numerical upscaling procedure proposed by Rubino et al. (2009) to compute the associated WIFF effects. That is, we impose a homogeneous time-harmonic vertical solid displacement of the form $-\Delta u\, e^{i\omega t}$ along the top boundary of the subsample (Figure 1b), where ω is the angular frequency. In addition, no-flow conditions are imposed on the four boundaries and no tangential forces are applied. The solid, on the other hand, is not allowed to move vertically on the bottom boundary nor to have horizontal displacements on the lateral boundaries. The response of the sample subjected to this relaxation test is obtained by solving Biot's (1941) consolidation equations under appropriate boundary conditions. Under the assumption that the volume average response of the sample can be represented with an equivalent homogeneous viscoelastic solid, an equivalent complex-valued frequency-dependent plane wave modulus is obtained, which permits to compute the seismic attenuation and phase velocity. We include in Appendix B the details of this numerical upscaling procedure.

It is important to notice here that Biot's (1941) theory locally considers the existence of a single pore fluid phase. However, during an imbibition experiment, each cell of the numerical rock sample can be saturated by a mixture of gas and water. In order to overcome this limitation, we locally employ an effective fluid phase when solving equations B1 – (B4). That is, following Rubino and Holliger (2012), at each computational cell containing a mixture of gas and water with saturations S_g and S_w, we define an effective single-phase fluid with properties determined by those of the individual fluid phases and weighted by their saturation values. The compressibility of the effective fluid is a crucial parameter in the WIFF process. As we consider computational cells having sizes much smaller than the diffusion lengths involved in the considered WIFF analysis, the pressure perturbations caused by the seismic wavefield have enough time to equilibrate within each computational cell. Hence, the fluid pressure within each cell is uniform and we can use Wood's law (Wood, 1955) to obtain the bulk modulus of the effective fluid

$$\frac{1}{K_f} = \frac{S_g}{K_g} + \frac{S_w}{K_w}, \tag{12}$$

where K_g and K_w are the bulk moduli of the gas and water, respectively.

On the other hand, following the work of Rubino and Holliger (2012), we use the relation of Teja and Rice (1981) to obtain the viscosity of the two-phase pore fluid mixture

$$\eta_f = \eta_g \left(\frac{\eta_w}{\eta_g}\right)^{S_w}. \tag{13}$$

It is important to remark here that although the effects of gravity and capillary pressure on the fluid distributions are taken into account when solving the two-phase flow equations, they are not considered when quantifying WIFF effects.

3. Numerical Analysis

3.1. Time Lapse Seismic Attenuation Estimates

We first subject the rock sample shown in Figure 1a to an imbibition experiment with a constant injection rate of $q_w^T = 1 \times 10^{-4}$ m/s upon achievement of a steady state. We consider an initial homogeneous saturation field mostly containing gas, with a water saturation value $S_w = 8\%$, which is slightly above the residual saturation considered in the analysis. For this test we select the fluid properties of water and methane gas, listed in Table 1. Also, we select a constant pressure of $p_w^B = 10$ MPa and a constant saturation of $S_w^B = 8\%$ as boundary conditions at the bottom. As previously mentioned, we analyze the evolution of the resulting gas-water distributions and of the associated seismic signatures of the subsample shown in Figure 1b.

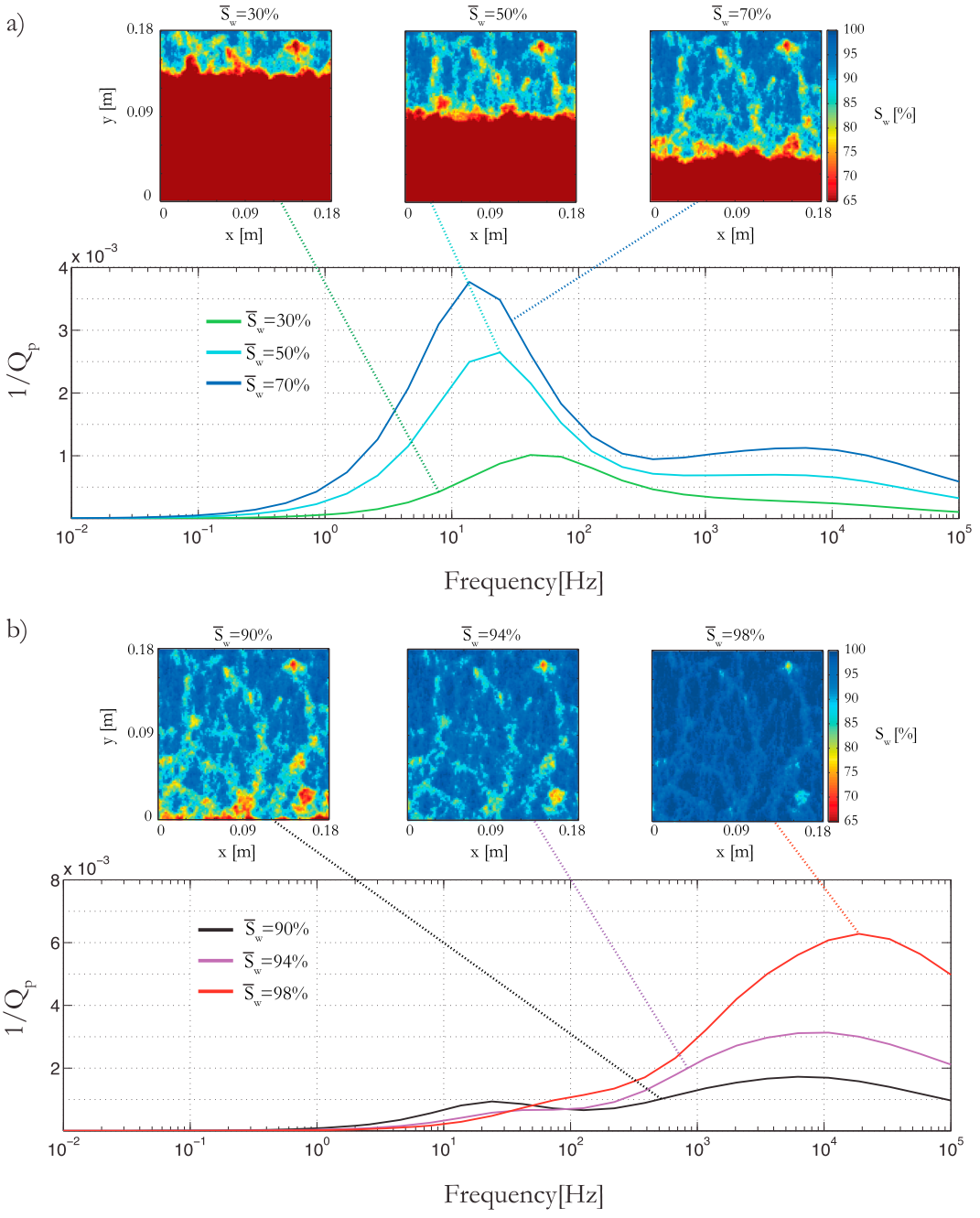

Figure 2. Water saturation fields obtained from the numerical imbibition experiment for a constant injection rate $q_w^T = 1 \times 10^{-4}$ m/s and associated inverse quality factor $1/Q_p$ as a function of frequency. (a) Green, light blue, and dark blue lines denote overall water saturation levels of 30%, 50%, and 70%, respectively ; (b) black, violet, and red lines denote overall water saturation levels of 90%, 94%, and 98%, respectively.

Figure 2a (top row) shows the evolution of the saturation fields as a result of the imbibition process. In order to characterize this evolution, we compute, in each case, the overall saturation of the sample

$$\overline{S}_w = \frac{\sum_{ij} S_w\left(\Omega_{ij}\right) \phi\left(\Omega_{ij}\right)}{\sum_{ij} \phi\left(\Omega_{ij}\right)}, \tag{14}$$

with Ω_{ij} denoting the ijth cell of the employed regular computational mesh. For a given overall saturation, we observe a clear transition between a region containing high values of water saturation and the rest of the sample containing mostly gas. The interface separating these two zones is commonly referred to as the saturation

front. We observe in Figure 2a that the front advances as the imbibition process evolves or, in other words, as the overall water saturation of the sample increases from $\bar{S}_w = 30\%$ to 70%. In detail, it can be seen that as water invades different regions of the heterogeneous sample, local values of water saturation increase and capillary pressure values drop, following equation (9). As each cell of the numerical rock sample is characterized by a distinct porosity, permeability, and capillary pressure curve, the geometrical patterns of the regions locally containing high values of water saturation behind the saturation front as well as the saturation front itself turn out to be heterogeneous. The resulting saturation field produces compressibility contrasts between the different parts of the sample, and, therefore, it may be associated with seismic attenuation due to WIFF. In order to explore this, Figure 2a (bottom) depicts, for the previously described stages of the imbibition process, the associated seismic attenuation as a function of frequency. We observe that indeed, seismic attenuation due to WIFF arises. Further inspection of the curves allows us to observe two attenuation peaks: one located at frequencies between 10 and 100 Hz and a second one at frequencies around 6 kHz. We observe that with increasing values of overall water saturation, the levels of attenuation of both peaks increase. Moreover, the first attenuation peak shifts toward lower frequencies with increasing values of overall water saturation.

Figure 2b shows the results for later stages of the imbibition process, for which the saturation front has passed through the subsample. We observe in Figure 2b (top row) that gas patches were trapped behind the front, and regions having locally very high levels of water saturation appear. Figure 2b (bottom) indicates that for these stages of the imbibition process, the first attenuation peak is virtually inexistent, whereas the level of attenuation of the second peak got stronger if compared to previous stages. Moreover, the second peak gets higher and shifts toward higher frequencies with increasing values of overall water saturation.

By comparing the attenuation curves shown in Figures 2a and 2b, it can be argued that the first attenuation peak is produced by the presence of the saturation front, whereas the second one is associated with residual patches located behind the saturation front. In the case of the low-frequency peak, the saturation front divides the medium into two layers with contrasting compressibilities, generating a spatial distribution that resembles White's double-layer model (White et al., 1975). On the other hand, the high-frequency peak is produced by the presence of regions with very high values of water saturation surrounded by zones containing a mixture of water and gas in the pore space. The numerical simulations show that the heterogeneous saturation distributions resulting from the imbibition experiment produce relatively low levels of seismic attenuation. Even though there is no consensus on the lowest measurable attenuation levels in laboratory experiments, according to Tisato and Madonna (2012) extensional attenuation values $1/Q_E$ above 0.003 can be measured. In addition, based on the works of Winkler and Nur (1979) and Spencer and Shine (2016), we conclude that $1/Q_p > 1/Q_E$ for the partially saturated rock samples considered in our analysis. This implies that the attenuation levels obtained in this subsection are, at best, experimentally measurable only for the first peak of the case $\bar{S}_w = 70\%$ (Figure 2a) and for the peaks arising in the cases $\bar{S}_w = 94\%$ and $\bar{S}_w = 98\%$ (Figure 2b).

It is important to recall that the saturation distribution of a porous sample depends on the characteristics of the injection process. In this sense, imbibition and drainage processes constitute two extreme regimes, which are characterized by particular capillary pressure and relative permeability curves (e.g., Soldi et al., 2017). This, in turn, generates a hysteresis effect, which has significant consequences for the associated seismic response (Le Ravalec et al., 1996; Yin et al., 1992; Zhang et al., 2015). In particular, imbibition experiments seem to be associated with lower levels of attenuation than drainage experiments (e.g., Cadoret et al., 1995, 1998). The general tendency to have low levels of seismic attenuation during imbibition processes observed in our simulations is due to the fact that as initially the whole sample contains very high values of gas saturation, it is very difficult to produce regions fully saturated with water. Regions that are fully, or almost fully, saturated with water are crucial for generating compressibility contrasts within the rock sample because the bulk modulus of the effective fluid is given by the harmonic average of the individual bulk moduli (equation (12)). Figure 3 shows the behavior of the bulk modulus of the effective fluid as a function of water saturation. Note that the local presence of very low amounts of gas is enough to produce a bulk modulus of the effective fluid very close to that of the gas. In other words, this implies that unless there are essentially fully water-saturated patches, the compressibility contrasts between the different parts of the sample tend to be rather weak and thus associated with low levels of WIFF attenuation.

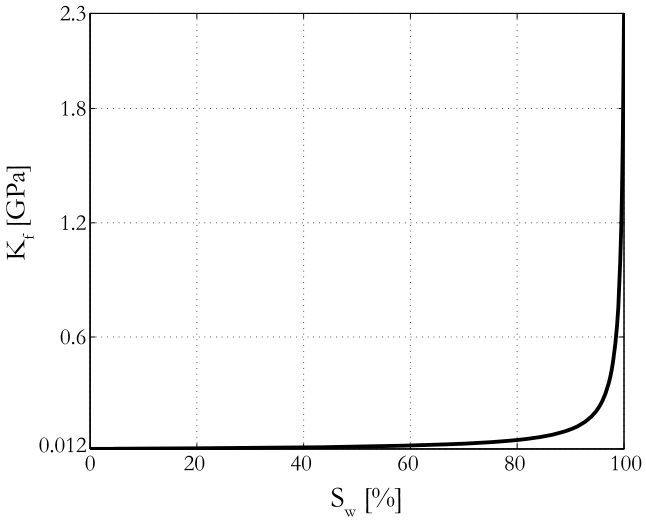

Figure 3. Bulk modulus of the effective fluid K_f as a function of water saturation S_w. Note that K_f varies from K_g to K_w for saturation levels ranging between 0% and 100%, respectively. The physical properties of gas and water are given in Table 1.

3.2. Physical Interpretation of the Attenuation Curves

In order to further explore the physical reasons for the attenuation behavior observed in Figure 2, we compute the local contribution to the overall seismic attenuation of the sample (Solazzi et al., 2016)

$$q_{ij}^{-1}(\omega) = \frac{\Delta \mathcal{P}_{ij}(\omega)}{2\delta^2 \omega \mathcal{W}(\omega)}. \tag{15}$$

In this equation, the parameter $\Delta \mathcal{P}_{ij}(\omega)$ denotes the local dissipated power averaged over one wave cycle of oscillation and can be computed as

$$\Delta \mathcal{P}_{ij}(\omega) = \omega^2 \left(\frac{\eta_f ||\boldsymbol{w}||^2}{2\kappa} \right)_{ij} \delta^2, \tag{16}$$

with δ^2 being the area of the cell Ω_{ij}, and $\boldsymbol{w}$ is the average relative fluid displacement. In addition, $\mathcal{W}(\omega)$ denotes the average strain energy over one wave cycle and is given by

$$\mathcal{W}(\omega) = \frac{\delta^2}{4} \sum_{ij} \Re \left\{ \boldsymbol{\sigma} : \boldsymbol{\epsilon}^* + p_f \xi^* \right\}_{ij}, \tag{17}$$

where $\boldsymbol{\sigma}$ is the stress tensor, $\boldsymbol{\epsilon}$ the strain tensor, p_f the fluid pressure, and $\xi = -\nabla \cdot \boldsymbol{w}$ the local change in fluid content. The symbol $*$ denotes the complex conjugate, : the double dot product of the corresponding tensors, and $\Re$ the corresponding real part. The spatial distribution of the parameter q_{ij}^{-1} allows us to determine the regions that effectively contribute to the overall attenuation.

The local contribution to attenuation for $\bar{S}_w = 70\%$ is displayed in Figures 4b and 4c, for frequencies of $f_{\text{low}} = 13.74$ Hz and $f_{\text{high}} = 6,210$ Hz, respectively. These two frequencies correspond to the approximate locations of the two attenuation peaks (Figure 2a). To facilitate the analysis, we include in Figure 4a the saturation distribution for this overall saturation. Comparing Figures 4a and 4b, we observe that for the frequency of the first attenuation peak, energy dissipation mainly occurs in the region located in the vicinity of the saturation front and containing high values of water saturation. Here there is an abrupt change from a zone characterized by high values of water saturation to another one mostly saturated with gas, which is responsible for a corresponding compressibility contrast and WIFF. In the case of the frequency of the second attenuation peak, energy dissipation occurs behind the saturation front (Figure 4c). Comparing Figures 4a and 4c, we observe that these dissipating zones correspond to the boundaries of patches characterized by very high values of water saturation. This analysis therefore demonstrates that as suggested before, the first attenuation peak observed in Figure 2a corresponds to the saturation contrast produced by the saturation front, whereas the second one is associated with regions having very high levels of water saturation and located behind the front.

Figure 4e shows the local contribution to attenuation for $\bar{S}_w = 98\%$ for a frequency of $f_{\text{high}} = 1.8 \times 10^4$ Hz, which corresponds to the location of the single attenuation peak that arose in this case (Figure 2b). We observe that significant energy dissipation arises. Comparisons between Figure 4d, where the corresponding saturation distribution is shown, and Figure 4e show that the regions where dissipation occurs correspond to the boundaries of patches characterized by very high levels of water saturation. Moreover, comparing Figures 4c and 4e, we observe that the presence of higher local values of water saturation for $\bar{S}_w = 98\%$ implies stronger compressibility contrasts with respect to the surrounding areas and, therefore, higher levels of attenuation. It is also interesting to note that as water saturation increases from $\bar{S}_w = 70\%$ to $\bar{S}_w = 98\%$, the fraction of the rock containing essentially fully water-saturated regions increases, which, in turn, also favors the increase of the attenuation levels.

The frequency associated with the attenuation peak is strongly influenced by the characteristic size of the heterogeneities that generate the fluid pressure relaxation (e.g., Müller et al., 2010). That is, maximum attenuation occurs at a frequency

$$f_{\text{max}} \simeq \frac{D}{2\pi a_{\text{meso}}^2}, \tag{18}$$

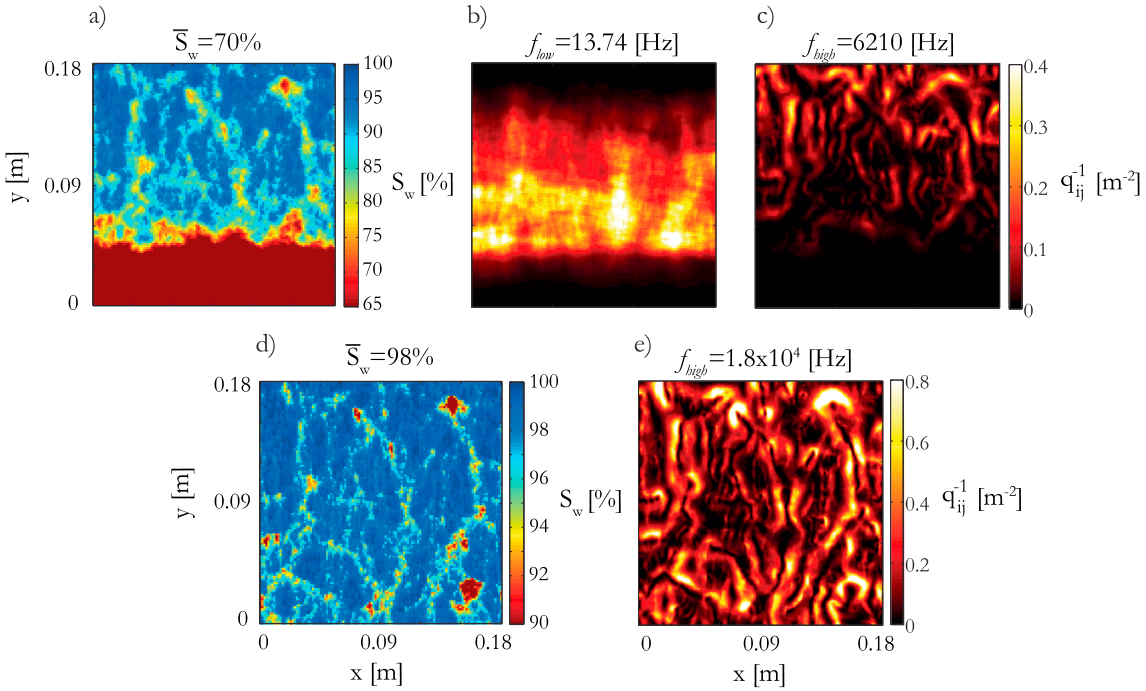

Figure 4. Spatial distribution of q_{ij}^{-1} for the sample subjected to a numerical imbibition experiment (a) for $\overline{S}_w$ = 70% computed at the frequency of the (b) first and (c) second attenuation peaks and that (d) for $\overline{S}_w$ = 98% computed at the (e) frequency of the associated single attenuation peak.

where D is the diffusivity of the medium, given by equation (B8), and a_{meso} is the characteristic size of the heterogeneities. As the size of the region having high levels of water saturation and associated with the front is larger than that of the isolated patches located behind the front, equation (18) implies that the attenuation peak related to the saturation front occurs at lower frequencies than that produced by the isolated patches. Equation (18) also explains the shift toward lower frequencies of the first peak with increasing overall water saturation of the sample (Figure 2a). That is, as the imbibition process evolves, the front advances and the associated region having high levels of water saturation grows. This implies that the characteristic size a_{meso} increases its value, and, therefore, f_{max} decreases. It is important to remark here that the diffusivity D is a parameter that depends on the physical properties of the matrix and the effective fluid. Indeed, this parameter assumes higher values as water saturation increases, and the increase rate is especially strong for situations close to $S_w = 100\%$. According to equation (18), this implies that the frequency associated with the attenuation peak should increase with the saturation. Thus, there is a competition between the effects produced by the size of the heterogeneity and those related to the local water saturation value. The results shown in Figure 2a indicate that in the case of the saturation front, the changes of a_{meso} play a more important role than the variations of D.

The attenuation peaks in Figure 2b, on the other hand, are associated with the presence of isolated patches characterized by high levels of water saturation. Interestingly, as the overall saturation of the sample increases from $\overline{S}_w$ = 90% to 98%, we observe that the frequency peak moves toward higher frequencies. Taking into account that both the size of the patches and the local levels of water saturation are expected to increase with increasing values of overall water saturation, the behaviors shown in Figure 2b indicate that in this case, the frequency shift is dominated by a local increase of the diffusivity.

Equation (18) also allows us to estimate the characteristic size of the heterogeneities by using approximate values of f_{max} and D. As an example, we can employ equation (18) to analyze the cases represented by Figures 4b and 4e. In each case, we select the corresponding peak frequency from Figure 2, and the fluid and host rock properties are computed for a mean porosity value of 0.3 following the procedure described in the work. Considering an approximate saturation of 0.8 for the region where energy dissipation occurs in the situation depicted by Figure 4b, we obtain, by means of an exhaustive search, a characteristic size for the heterogeneities $a_{\text{meso}} \simeq 6$ cm. It is interesting to notice that this size is comparable to the thickness of the

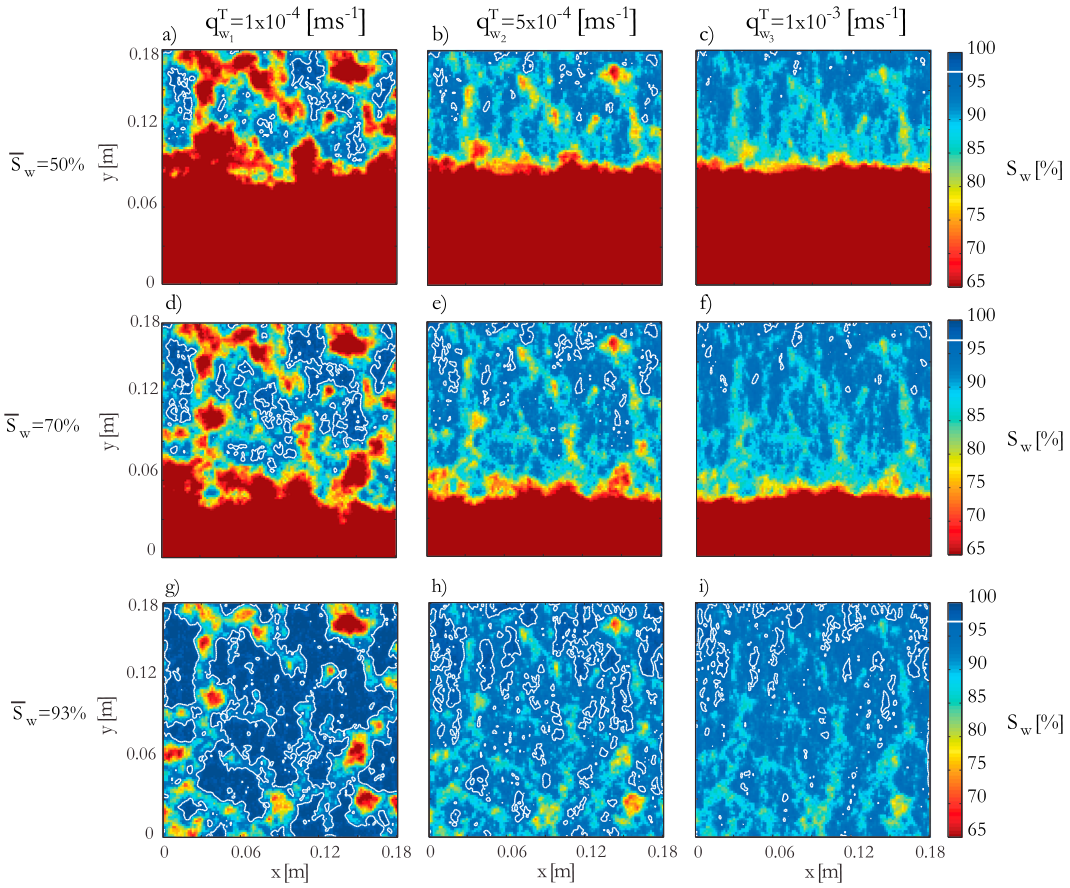

Figure 5. Water saturation fields resulting from numerical imbibition experiments with injection rates of (a, d, g) $q^T_{w_1} = 1 \times 10^{-4}$ m/s, (b, e, h) $q^T_{w_2} = 5 \times 10^{-4}$ m/s, and (c, f, i) $q^T_{w_3} = 1 \times 10^{-3}$ m/s. The different rows correspond to different instants of the imbibition processes characterized by overall water saturation levels of $\overline{S}_w = 50\%$ (Figures 5a–5c), $\overline{S}_w = 70\%$ (Figures 5d–5f), and $\overline{S}_w = 93\%$ (Figures 5g–5i). White contour lines delimit the regions where local water saturation is above 97%.

region responsible for the overall attenuation (Figure 4b). Conversely, considering a saturation of 0.99 for the patches controlling the energy dissipation shown in Figure 4e, we obtain a characteristic size of $a_{meso} \simeq 0.5$ cm. By comparing Figures 4d and 4e, we observe that also in this case this characteristic size is representative of the water-saturated patches that effectively contribute to the overall attenuation of the sample.

3.3. Injection Rate Effects on Seismic Attenuation

The flow regime of imbibition processes is determined by the balance between viscous, gravitational, and capillary forces (Lopes et al., 2014; Riaz et al., 2007). The injection rate is a crucial parameter because it affects the relation between these forces and, thus, it partly determines the evolution of the saturation field within the porous sample (Helmig et al., 2006). In the following, we explore the effects of changing the injection rate on the characteristics of the fluid distributions and the impact on the associated seismic attenuation due to WIFF. Hence, we repeat the analysis presented in the previous subsection but considering three different injection rates: $q^T_{w_1} = 1 \times 10^{-4}$ m/s, $q^T_{w_2} = 5 \times 10^{-4}$ m/s, and $q^T_{w_3} = 1 \times 10^{-3}$ m/s. The employed rock sample and physical properties remain unchanged.

Figure 5 shows the resulting water saturation fields, with columns from left to right corresponding to increasing values of water injection rates. Moreover, the rows correspond to different overall water saturation of the sample, with increasing values from top to bottom. Given the importance of regions with locally very high levels of water saturation for producing WIFF effects, we include in each panel a white contour line to delimit the regions where local water saturation is above 97%. This corresponds to a bulk modulus of 0.35 GPa for the effective fluid, as indicated by Figure 3.

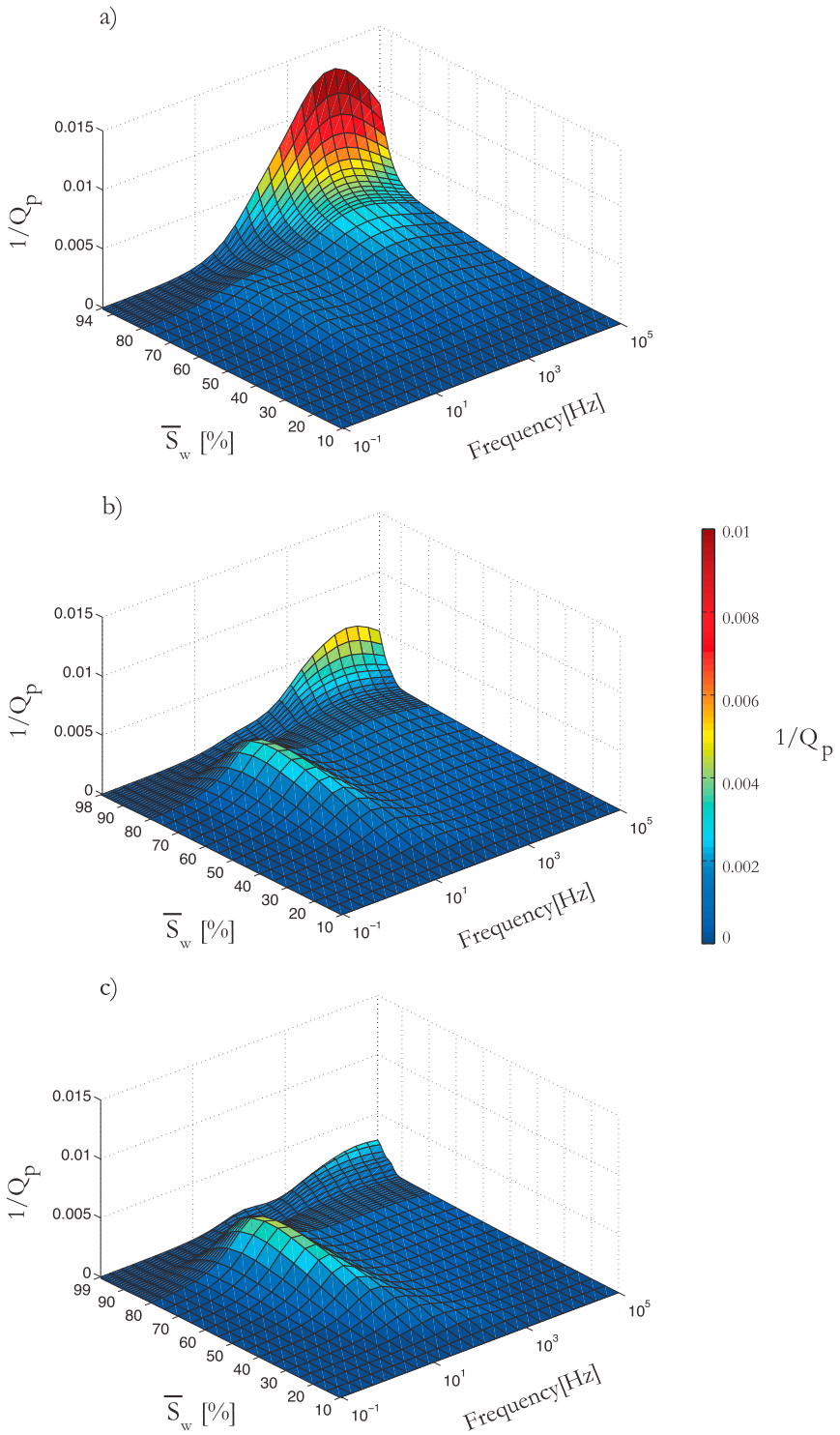

Figure 6. Inverse *P* wave quality factor $1/Q_p$ as a function of overall water saturation and frequency for the fluid distributions obtained with injection rates of (a) $q^T_{w_1} = 1 \times 10^{-4}$ m/s, (b) $q^T_{w_2} = 5 \times 10^{-4}$ m/s, and (c) $q^T_{w_3} = 1 \times 10^{-3}$ m/s.

We observe in Figure 5 that as the injection rate increases, the saturation fields change from an injection process with substantial gas and water trapping and an irregular saturation front (Figures 5a, 5d, and 5g) to one where the main characteristic is the presence of a sharp saturation front (Figures 5c, 5f, and 5i). The reason for this is that when the imbibition process is characterized by a slow injection rate, the induced pressure gradients are rather weak. Hence, the invading phase tends to flow through preferential paths, where there is less resistance to the flow. Consequently, the imbibition process presents a dendritic saturation front. In this scenario, regions with very high local water saturation levels are formed behind the front, as observed in Figures 5a, 5d, and 5g. Conversely, when the imbibition process is characterized by a high injection rate, the induced pressure gradients generate a rapid saturation of all the regions of the probed sample. Correspondingly, the invading phase evolves following a compact piston-like displacement, as evidenced in Figures 5c, 5f, and 5i. We observe that behind the front, patches with high values of water saturation are rather absent and tend to appear for very high values of overall water saturation.

Seismic waves are expected to respond to the evolution of the saturation field in each imbibition process differently. In order to explore this, we include in Figure 6 the resulting *P* wave attenuation as a function of overall water saturation and frequency for the three injection rates employed in Figure 5. Please note that each numerical imbibition process reaches a different maximum overall saturation value. We observe that at very low injection rates, the low-frequency peak associated with the saturation front is not significant (Figure 6a). This is possibly due to the fact that for such low injection rates, the saturation front is rather irregular and, thus, the pressure relaxation process taking place at a certain region of the front tends to interact with those arising in the surrounding regions, which in turn diminishes WIFF effects. Conversely, the attenuation peak produced by isolated water patches formed behind the saturation front is significant, with Q values below 100 for $\bar{S}_w$ values above 90%. The importance of this manifestation of WIFF is related to the fact that the considered slow injection rate favors the formation of patches having high values of local water saturation behind the saturation front, which creates strong compressibility contrast and WIFF.

When we increase the injection rate, seismic attenuation experiences significant changes, as shown in Figures 6b and 6c. We observe that a low-frequency peak arises for overall saturations ranging from 30% to 80% and increases its magnitude with increasing injection rate. Note that this low-frequency peak presents a transient behavior. That is, it grows as both the characteristic size of saturation front and the compressibility contrast increase, and, finally, it disappears once the saturation front has passed through the sample. In addition, as a higher injection rate hinders the formation of patches with high water saturation values behind the saturation front, the associated high-frequency peak is reduced, as depicted by Figures 6b and 6c.

4. Discussion

To our knowledge, little work has so far been done to study in detail the causes of seismic attenuation observed during imbibition processes in general and the role of the injection rate in particular. Our numerical analysis indicates that the heterogeneous saturation fields produced during imbibition processes and related to subsample-scale heterogeneities can lead to measurable levels of seismic attenuation due to WIFF. In particular, we observe in Figure 6 that this dissipation mechanism gets more significant for overall water saturations greater than 90%. This is in correspondence with laboratory measurements of seismic attenuation (e.g., Murphy, 1984; Tisato & Quintal, 2013; Winkler & Nur, 1979; Yin et al., 1992). For example, Yin et al. (1992) performed imbibition experiments in a Berea sandstone and observed an attenuation peak located at ~97% brine saturation. They attributed the frequency-dependent behavior of seismic attenuation to WIFF taking place between isolated patches formed during the imbibition experiment. More recently, Tisato and Quintal (2013) studied seismic attenuation in a partially saturated Berea sandstone for increasing water saturation values. They observed frequency-dependent attenuation for overall water saturation values of 86.5% and 97.1%, and they argued that it was generated by mesoscopic WIFF due to a heterogeneous pore fluid distribution.

It is important to notice here that while the Q values observed in the laboratory experiments considered in the above mentioned studies are approximately 25, our simulations only produce values of 80 or higher. To explore this discrepancy between the attenuation levels, we have performed an exhaustive analysis considering different lithologies, pore fluids for the nonwetting phase (methane, CO_2, and air), porosity-elastic moduli relations, and properties of the stochastic porosity field, and the general levels of seismic attenuation turned out to be similar to or below those included in this work. In this context, it should be noticed that

we compute Q_p^{-1} using the complex-valued frequency-dependent equivalent modulus M_c, while the above mentioned studies compute extensional attenuation Q_E^{-1} using the complex-valued frequency-dependent equivalent Young's modulus E. The equivalent Young's modulus and the extensional attenuation can be calculated as (Tisato & Quintal, 2013)

$$E = \mu_c \frac{(3M_c - 4\mu_c)}{M_c - \mu_c}, \quad Q_E^{-1} = \frac{\Im\{E\}}{\Re\{E\}}, \tag{19}$$

where μ_c is the equivalent shear modulus of the heterogeneous saturated sample and $\Im$ denotes the corresponding imaginary part. In our case, an approximation of E can be obtained by considering a constant μ_c, equal to the mean shear modulus of the dry frame. This assumption is supported by the fact that the main contrasting heterogeneities present in our numerical simulations are related to the fluid saturation field and not to the rock properties. This approach leads to Q_E^{-1} values for our simulations that are ~40% lower than those of Q_p^{-1} which, in other words, implies that the discrepancies between the attenuation levels simulated in this work and those observed in laboratory experiments are even more dramatic. These discrepancies therefore suggest that other energy dissipation mechanisms, such as squirt flow or anelasticity of the dry frame, are expected to play a predominant role during imbibition processes. Some of these attenuation mechanisms produced by microscopic characteristics of the rock frame can be incorporated into the numerical upscaling procedure by employing complex-valued frequency-dependent bulk and shear moduli of the rock dry frame, as proposed by Rubino and Holliger (2012).

Due to computational limitations, the analysis presented in this work has been limited to 2-D. Although the associated assumptions with regard to the third dimension may indeed cause artifacts, the overall nature of the results obtained in this paper is expected to remain valid. In this context, it is important to remark that the attenuation behaviors derived from the numerical upscaling procedure can be considered comparable with those obtained from laboratory subresonance experiments (e.g., Tisato & Madonna, 2012). Conversely, during laboratory attenuation estimates based on the transmission of a seismic pulse, the attenuation peak produced by the saturation front cannot be seen. Instead, the saturation front could be interpreted in the seismic data as a reflective interface. The patches containing high levels of water saturation and located behind the saturation front, on the other hand, could produce seismic attenuation due to WIFF. For sufficiently high frequencies, however, instead of producing attenuation due to WIFF, they will generate scattering. In addition, although the numerical analysis included in this work considers heterogeneous distributions of the properties of the dry rock frame, the general findings are expected to be applicable to imbibition experiments applied to rocks considered to be homogeneous. This statement is based on the fact that permeability is a highly fluctuating parameter, which can vary over several orders of magnitude in short distances and whose local determination within a porous rock is very difficult to achieve. Indeed, the permeability value commonly inferred from flow tests in laboratory experiments corresponds to an effective hydraulic permeability at the sample's scale, but no detailed information on the permeability fluctuations possibly occurring at subsample scale is provided. Taking into account that permeability is a key parameter controlling the fluid distributions in response to imbibition experiments, heterogeneous saturation fields with characteristics comparable to those observed in the numerical simulations are expected to arise.

It is clear from our numerical analysis that besides the overall saturation value, the detailed geometrical characteristics of the fluids patches are of great importance with respect to the associated seismic attenuation due to WIFF. As shown in Figure 5, different injection rates generate different distributions of gas patches for the same overall saturation value. The impact of the injection rate on the generation of fluid patches can be analyzed by means of the capillary number C_a. This dimensionless number is used to quantify the ratio of viscous to capillary forces. There are different definitions for the capillary number; however, for a Darcy-scale process it can be expressed as (Hilfer & Øren, 1996)

$$C_a = \frac{\eta_w \bar{q}_w \bar{l}}{\bar{\kappa}\, \bar{p}_d}, \tag{20}$$

where $\bar{l}$, $\bar{q}_w$, $\bar{p}_d$, and $\bar{\kappa}$ are characteristic values for the sample length, the Darcy velocity of the wetting phase, the entry pressure, and the rock permeability, respectively. If an injection process has a capillary number greater than 1, the viscous forces dominate the displacement. Conversely, if $C_a < 1$, capillary forces dominate the fluid displacement (Armstrong et al., 2014). We take $\bar{l}$ as the length of the subsample, $\bar{q}_w$ as the injection

rate, and $\overline{\kappa}$ and $\overline{p}_d$ as the arithmetic mean of the permeability and entry pressure computed within the subsample, respectively. We obtain three capillary numbers, $C_{a_1} = 0.45$, $C_{a_2} = 2.24$, and $C_{a_3} = 4.45$, in correspondence with the chosen injection rates, $q^T_{w_1} = 1\times10^{-4}$ m/s, $q^T_{w_2} = 5\times10^{-4}$ m/s, and $q^T_{w_3} = 1\times10^{-3}$ m/s. Our results show that viscous-dominated imbibition processes are characterized by a sharp saturation front discontinuity (Figures 5c, 5f, and 5i) and, thus, present an associated dominating attenuation peak that shifts toward lower frequencies with increasing overall saturation values (Figure 6c). This manifestation of WIFF can arise while the saturation front is present in the sample. For capillary-dominated processes, on the other hand, the saturation fields are characterized by substantial water and gas trapping and an irregular saturation front (Figures 5a, 5d, and 5g). The associated seismic attenuation is mainly due to WIFF between isolated patches with very high levels of water saturation and their surroundings. Our numerical analysis indicates that the corresponding attenuation peak shifts toward higher frequencies with increasing values of overall water saturation of the sample (Figure 6a). These contrasting behaviors indicate that it may be possible to discern whether a given imbibition process is capillary dominated or viscous dominated by observing the evolution of the associated seismic attenuation signatures.

5. Conclusions

In this paper, we have implemented a numerical procedure to emulate a laboratory-based forced imbibition process in a heterogeneous sandstone sample. We then selected a subsample of the considered rock and, employing the resulting time-dependent saturation fields, we applied a numerical upscaling procedure to quantify seismic attenuation due to WIFF. Based on this joint approach, we performed a comprehensive numerical analysis to explore the geometrical characteristics of the fluid distributions in response to imbibition experiments, the impact on seismic attenuation, and the role played by the injection rate.

Our results showed that measurable levels of seismic attenuation due to WIFF can arise during imbibition processes, especially for high values of overall water saturation. Moreover, two attenuation peaks can arise. Analysis of the local contribution to the overall seismic attenuation allowed us to demonstrate that the first attenuation peak is produced by the compressibility contrast related to the presence of the saturation front and tends to appear during viscous-dominated imbibition processes, which are produced by high injection rates. Moreover, this attenuation peak vanishes when the saturation front has passed through the sample. The second attenuation peak, on the other hand, arises at higher seismic frequencies and is produced by the presence of patches characterized by very high local levels of water saturation located behind the saturation front. This manifestation of WIFF plays an important role during capillary-dominated processes, that is, for relatively low injection rates. The magnitude of the attenuation peaks produced by the two manifestations of WIFF tends to increase with increasing overall water saturation. However, while the peak produced by the saturation front shifts toward lower frequencies with increasing overall water saturation, the one related to patches of high water saturation shifts toward higher frequencies. The results of this work, in combination with the proposed joint numerical approach, constitute a useful framework for the interpretation of seismic attenuation in partially saturated formations in general and during forced imbibition experiments in particular.

Appendix A: Boundary Conditions Related to the Two-Phase Fluid Flow Simulations

To obtain the saturation distribution of a numerical rock sample subjected to a forced imbibition procedure, equations (5)–(11) are solved using a finite element procedure under corresponding initial and boundary conditions. Let $\Omega = L_x \times L_y$ be a domain that represents the probed sample. In addition, Γ is the boundary of Ω, which is given by $\Gamma = \Gamma^L \cup \Gamma^B \cup \Gamma^R \cup \Gamma^T$, where

$$\Gamma^L = \{(x,y) \in \Omega : \ x = 0\}, \tag{A1}$$

$$\Gamma^R = \{(x,y) \in \Omega : \ x = L_x\}, \tag{A2}$$

$$\Gamma^B = \{(x,y) \in \Omega : \ y = 0\}, \tag{A3}$$

$$\Gamma^T = \left\{(x,y) \in \Omega : \ y = L_y\right\}. \tag{A4}$$

Moreover, ν denotes the unit outer normal on Γ and χ is a unit tangent so that $\{\nu, \chi\}$ is an orthonormal system on Γ.

To solve the two-phase flow equations, we consider the initial condition

$$S_w = 8\% \quad (x,y) \in \Omega, \tag{A5}$$

and boundary conditions

$$\boldsymbol{q_w} \cdot \boldsymbol{\nu} = -q_w^T, \quad (x,y) \in \Gamma^T, \tag{A6}$$

$$\boldsymbol{q_w} \cdot \boldsymbol{\nu} = 0, \quad (x,y) \in \Gamma^L \cup \Gamma^R, \tag{A7}$$

$$\boldsymbol{q_n} \cdot \boldsymbol{\nu} = 0, \quad (x,y) \in \Gamma^T \cup \Gamma^L \cup \Gamma^R, \tag{A8}$$

$$p_w = 10\,\text{MPa}, \quad (x,y) \in \Gamma^B, \tag{A9}$$

$$S_w = 8\%, \quad (x,y) \in \Gamma^B. \tag{A10}$$

Appendix B: Numerical Oscillatory Relaxation Test for Computing Seismic Attenuation Due To WIFF

To compute the response of the sample subjected to the relaxation test, we solve Biot's (1941) quasi-static poroelastic equations, which in the space frequency domain results in the following system of equations

$$\nabla \cdot \boldsymbol{\sigma} = 0, \tag{B1}$$

$$\nabla p_f = -i\omega \frac{\eta}{\kappa} \boldsymbol{w}. \tag{B2}$$

Equations (B1) and (B2) are coupled through the stress-strain constitutive relations (Biot, 1962)

$$\boldsymbol{\sigma} = 2\mu_m \boldsymbol{\epsilon} + \boldsymbol{I}\left(\lambda_c \nabla \cdot \boldsymbol{u} - \alpha M \zeta\right), \tag{B3}$$

$$p_f = -\alpha M \nabla \cdot \boldsymbol{u} + M\zeta, \tag{B4}$$

where $\boldsymbol{I}$ is the identity matrix and $\boldsymbol{u}$ the average solid displacement. The strain tensor is given by $\boldsymbol{\epsilon} = \frac{1}{2}\left(\nabla \boldsymbol{u} + (\nabla \boldsymbol{u})^{\mathrm{T}}\right)$, with T denoting the transpose operator. The poroelastic Biot-Willis parameter α, the fluid storage coefficient M, and the Lamé parameter λ_c are given by (e.g., Rubino et al., 2009)

$$\alpha = 1 - \frac{K_m}{K_s}, \tag{B5}$$

$$M = \left(\frac{\alpha - \phi}{K_s} + \frac{\phi}{K_f}\right)^{-1}, \tag{B6}$$

$$\lambda_c = K_m + \alpha^2 M - \frac{2}{3}\mu_m. \tag{B7}$$

The diffusivity D, employed in equation (18), can be expressed in terms of the poroelastic properties of the fluid-saturated porous rock (e.g., Rubino & Holliger, 2012)

$$D = \frac{\kappa}{\eta_f}\left(\frac{ML - \alpha^2 M^2}{L}\right), \tag{B8}$$

with $L = \lambda_c + 2\mu_m$.

Equations (B1)–(B4) are numerically solved under corresponding boundary conditions. Let Ω_{sub} be a domain that represents the sample subjected to the oscillatory test. In addition, Γ_{sub} is the boundary of Ω_{sub}. We consider the following boundary conditions

$$\boldsymbol{u} \cdot \boldsymbol{\nu}_{sub} = -\Delta u, \quad (x, y) \in \Gamma^{T}_{sub}, \tag{B9}$$

$$\boldsymbol{u} \cdot \boldsymbol{\nu}_{sub} = 0, \quad (x, y) \in \Gamma^{L}_{sub} \cup \Gamma^{R}_{sub} \cup \Gamma^{B}_{sub}, \tag{B10}$$

$$\left(\boldsymbol{\sigma} \cdot \boldsymbol{\nu}_{sub}\right)^{\mathsf{T}} \cdot \boldsymbol{\chi}_{sub} = 0, \quad (x, y) \in \Gamma_{sub}, \tag{B11}$$

$$\boldsymbol{w} \cdot \boldsymbol{\nu}_{sub} = 0, \quad (x, y) \in \Gamma_{sub}, \tag{B12}$$

where Γ^{L}_{sub}, Γ^{R}_{sub}, Γ^{B}_{sub}, and Γ^{T}_{sub} are the left, right, bottom, and top boundaries of the sample, respectively, and $\boldsymbol{\nu}_{sub}$ and $\boldsymbol{\chi}_{sub}$ are the unit normal and the unit tangent of the sample's boundary Γ_{sub}, respectively.

A finite element procedure is then employed to solve equations (B1)–(B4) under the previously described boundary conditions. We use bilinear functions to approximate the solid displacement vector and a closed subspace of the vector part of the Raviart-Thomas-Nedelec space of zero order for representing the relative fluid displacement (Nedelec, 1980; Raviart & Thomas, 1977). Assuming that the average response of the probed sample can be represented by an equivalent homogeneous isotropic viscoelastic solid, the resulting averages over the sample's volume of the vertical components of the stress and strain fields, $\langle \sigma_{yy}(\omega) \rangle$ and $\langle \epsilon_{yy}(\omega) \rangle$, allow to compute a complex-valued frequency-dependent equivalent plane wave modulus

$$M_c(\omega) = \frac{\langle \sigma_{yy}(\omega) \rangle}{\langle \epsilon_{yy}(\omega) \rangle}. \tag{B13}$$

The P wave inverse quality factor $1/Q_p$ is then given by (e.g., Solazzi et al., 2016)

$$\frac{1}{Q_p} = \frac{\Im\{M_c(\omega)\}}{\Re\{M_c(\omega)\}}. \tag{B14}$$

Acknowledgments
This work was supported by a grant from the Consejo Nacional de Investigaciones Científicas y Técnicas (CONICET) and has in part been completed within the Swiss Competence Center for Energy Research-Supply of Electricity with support of the Swiss Commission for Technology and Innovation (CTI). Santiago G. Solazzi thanks Leonardo B. Monachesi for enlightening discussions during the early stages of this work. We would like to thank Yves Guéguen and an anonymous reviewer for their insightful comments that greatly improved our manuscript. The data derived by the numerical simulations and the underlying models can be obtained free of charge upon request from the lead author.

References

Alemu, B. L., Aker, E., Soldal, M., Johnsen, Ø., & Aagaard, P. (2013). Effect of sub-core scale heterogeneities on acoustic and electrical properties of a reservoir rock: A CO_2 flooding experiment of brine saturated sandstone in a computed tomography scanner. *Geophysical Prospecting*, *61*, 235–250.

Armstrong, R. T., Georgiadis, A., Ott, H., Klemin, D., & Berg, S. (2014). Critical capillary number: Desaturation studied with fast X-ray computed microtomography. *Geophysical Research Letters*, *41*, 55–60. https://doi.org/10.1002/2013GL058075

Bear, J. (1972). *Dynamics of fluids in porous media*. New York: American Elsevier.

Biot, M. A. (1941). General theory of three-dimensional consolidation. *Journal of Applied Physics*, *12*(2), 155–164. https://doi.org/10.1063/1.1712886

Biot, M. A. (1962). Mechanics of deformation and acoustic propagation in porous media. *Journal of Applied Physics*, *33*(4), 1482–1498. https://doi.org/10.1063/1.1728759

Brooks, R., & Corey, A. (1964). *Hydraulic properties of porous media*, Hydrology Papers No. 3. Fort Collins, CO: Colorado State University.

Burdine, N. (1953). Relative permeability calculations from pore size distribution data. *Journal of Petroleum Technology*, *5*(3), 71–78.

Cadoret, T., Marion, D., & Zinszner, B. (1995). Influence of frequency and fluid distribution on elastic wave velocities in partially saturated limestones. *Journal of Geophysical Research*, *100*(B6), 9789–9803.

Cadoret, T., Mavko, G., & Zinszner, B. (1998). Fluid distribution effect on sonic attenuation in partially saturated limestones. *Geophysics*, *63*(1), 154–160.

Carman, P. (1937). Fluid flow through a granular bed. *Transactions of the Institution of Chemical Engineers*, *15*, 150–167.

Courant, R., Friedrichs, K., & Lewy, H. (1928). Über die partiellen Differenzengleichungen der mathematischen Physik. *Mathematische Annalen*, *100*(1), 32–74. https://doi.org/10.1007/BF01448839

Helmig, R., Miller, C. T., Jakibs, H., Class, H., Hilpert, M., Kees, C. E., & Niessner, J. (2006). Multiphase flow and transport modeling in heterogeneous porous media. In A. Di Bucchianico, R. Mattheij, & M. Peletier (Eds.), *Progress in industrial mathematics at ECMI 2004* (pp. 449–488). Berlin, Germany: Springer.

Hilfer, R., & Øren, P. E. (1996). Dimensional analysis of pore scale and field scale immiscible displacement. *Transport in Porous Media*, *22*(1), 53–72.

Hoteit, H., & Firoozabadi, A. (2008). Numerical modeling of two-phase flow in heterogenous permeable media with different capillarity pressures. *Advances in Water Resources*, *31*, 56–73.

Johnson, D. L. (2001). Theory of frequency dependent acoustics in patchy-saturated porous media. *The Journal of the Acoustical Society of America*, *110*, 682–694. https://doi.org/10.1121/1.1381021

Kozeny, J. (1927). Über kapillare leitung des wassers im boden. *Wien, Akademie der Wissenschaften*, *136*(2a), 271–306.

Kuteynikova, M., Tisato, N., Jänicke, R., & Quintal, B. (2014). Numerical modeling and laboratory measurements of seismic attenuation in partially saturated rock. *Geophysics*, *79*, L13–L20. https://doi.org/10.1190/GEO2013-0020.1

Le Ravalec, M., Guéguen, Y., & Chelidze, T. (1996). Elastic wave velocities in partially saturated rocks: Saturation hysteresis. *Journal of Geophysical Research*, *101*, 837–844.

Lenormand, R. (1990). Liquids in porous media. *Journal of Physics: Condensed Matter*, *2*, 79–88.

Lenormand, R., & Zarcone, C. (1984). Role of roughness and edges during imbibition in square capillaries. In *SPE Annual Technical Conference and Exhibition*. Houston, TX: Society of Petroleum Engineers.

Leverett, M. (1941). Capillary behavior in porous solids. *Transactions of the AIME Petroleum Engineering Division*, *69*, 142–152.

Liu, J., Müller, T. M., Qi, Q., Lebedev, M., & Sun, W. (2016). Velocity-saturation relation in partially saturated rocks: Modelling the effect of injection rate changes. *Geophysical Prospecting*, *64*(4), 1054–1066.

Lopes, S., & Lebedev, M. (2012). Research note: Laboratory study of the influence of changing the injection rate on the geometry of the fluid front and on *P*-wave ultrasonic velocities in sandstone. *Geophysical Prospecting*, *28*(1), 24–27.

Lopes, S., Lebedev, M., Müller, T. M., Clennell, M. B., & Gurevich, B. (2014). Forced imbibition into a limestone: Measuring *P*-wave velocity and water saturation dependence on injection rate. *Geophysical Prospecting*, *62*(5), 1126–1142.

Mair, R. W., Wong, G. P., Hoffmann, D., Hürlimann, M. D., Patz, S., Schuartz, L. M., & Walsworth, R. L. (1999). Probing porous media with gas diffusion NMR. *Physical Review Letters*, *83*(16), 3324–3327.

Masson, T. J., & Pride, S. R. (2007). Poroelastic finite difference modeling of seismic attenuation and dispersion due to mesoscopic-scale heterogeneity. *Journal of Geophysical Research*, *112*, B03204. https://doi.org/10.1029/2006JB004592

Masson, Y. J., & Pride, S. R. (2011). Seismic attenuation due to patchy saturation. *Journal of Geophysical Research*, *116*, B0326. https://doi.org/10.1029/2010JB007983

Mavko, G., Mukerji, T., & Dvorkin, J. (2009). *The rock physics handbook: Tools for seismic analysis of porous media*. Cambridge, UK: Cambridge University Press.

Müller, T. M., Gurevich, B., & Lebedev, M. (2010). Seismic wave attenuation and dispersion resulting from wave-induced flow in porous rocks—A review. *Geophysics*, *75*, 147–164. https://doi.org/10.1190/1.3463417

Murphy, W. (1984). Acoustic measures of partial gas saturation in tight sandstones. *Journal of Geophysical Research*, *89*, 11,549–11,559.

Nedelec, J. C. (1980). Mixed finite elements in r^3. *Numerische Mathematik*, *35*, 315–341. https://doi.org/10.1007/BF01396415

Pini, R., & Benson, S. M. (2017). Capillary pressure heterogeneity and hysteresis for the supercritical CO_2/water system in a sandstone. *Advances in Water Resources*, *108*, 277–292. https://doi.org/10.1016/j.advwatres.2017.08.011

Pride, S. R. (2005). Relationships between seismic and hydrological properties. In Y. Rubin & S. Hubbard (Eds.), *Hydrogeophysics* (pp. 253–290). Dordrecht, Netherlands: Springer.

Pride, S. R., & Berryman, J. G. (2003). Linear dynamics of double-porosity dual-permeability materials I. Governing equations and acoustic attenuation. *Physical Review E*, *68*, 36603.

Pride, S. R., Berryman, J. G., & Harris, J. M. (2004). Seismic attenuation due to wave-induced flow. *Journal of Geophysical Research*, *109*, B01201. https://doi.org/10.1029/2003JB002639

Qi, Q., Müller, T. M., Gurevich, B., Lopes, S., Lebedev, M., & Caspari, E. (2014). Quantifying the effect of capillarity on attenuation and dispersion in patchy-saturated rocks. *Geophysics*, *79*, WB35–WB50.

Raviart, P., & Thomas, J. (1977). Mixed finite element method for 2nd order elliptic problems. *Lecture Notes in Mathematics*, *606*, 292–315. https://doi.org/10.1007/BFb0064470

Ren, Q. Y., Chen, G. J., Yan, W., & Guo, T. M. (2000). Interfacial tension of (CO_2 + CH_4) + water from 298 K to 373 K and pressures up to 30 MPa. *Journal of Chemical and Engineering Data*, *45*(4), 610–612. https://doi.org/10.1021/je990301s

Renaud, G., Rivière, J., Le Bas, P.-Y., & Johnson, P. A. (2013). Hysteretic nonlinear elasticity of Berea sandstone at low-vibrational strain revealed by dynamic acousto-elastic testing. *Geophysical Research Letters*, *40*, 715–719. https://doi.org/10.1002/grl.50150

Riaz, A., Tang, G. Q., Tchelepi, H. A., & Kovscek, A. R. (2007). Forced imbibition in natural porous media: Comparison between experiments and continuum models. *Physical Review E*, *75*(3), 36305.

Rubino, J. G., & Holliger, K. (2012). Seismic attenuation and velocity dispersion in heterogeneous partially saturated porous rocks. *Geophysical Journal International*, *188*, 1088–1102. https://doi.org/10.1111/j.1365-246X.2011.05291.x

Rubino, J. G., Ravazzoli, C. L., & Santos, J. E. (2009). Equivalent viscoelastic solids for heterogeneous fluid-saturated porous rocks. *Geophysics*, *74*, N1–N13. https://doi.org/10.1190/1.3008544

Rubino, J. G., Velis, D. R., & Sacchi, M. D. (2011). Numerical analysis of wave-induced fluid flow effects on seismic data: Application to monitoring of CO_2 storage at the Sleipner field. *Journal of Geophysical Research*, *116*, 1088–1102. https://doi.org/10.1029/2010JB007997

Shi, J., Xue, Z., & Durucan, S. (2011). Supercritical CO_2 core flooding and imbibition in Tako sandstone—Influence of sub-core scale heterogeneity. *International Journal of Greenhouse Gas Control*, *5*, 75–87. https://doi.org/10.1016/j.ijggc.2010.07.003

Solazzi, S. G., Rubino, J. G., Müller, T. M., Milani, M., Guarracino, L., & Holliger, K. (2016). An energy-based approach to estimate seismic attenuation due to wave-induced fluid flow in heterogeneous poroelastic media. *Geophysical Journal International*, *207*(2), 823–832.

Soldi, M., Guarracino, L., & Jougnot, D. (2017). A simple hysteretic constitutive model for unsaturated flow. *Transport in Porous Media*. https://doi.org/10.1007/s11242-017-0920-2

Spencer, J. W., & Shine, J. (2016). Seismic attenuation and modulus dispersion in sandstones. *Geophysics*, *81*(3), D219–D239. https://doi.org/10.1190/GEO2015-0342.1

Teja, A. S., & Rice, P. (1981). Generalized corresponding states method for viscosities of liquid mixtures. *Industrial and Engineering Chemistry Fundamentals*, *20*, 77–81.

Tisato, N., & Madonna, C. (2012). Attenuation at low seismic frequencies in partially saturated rocks: Measurements and description of a new apparatus. *Journal of Applied Geophysics*, *86*, 44–53.

Tisato, N., & Quintal, B. (2013). Measurements of seismic attenuation and transient fluid pressure in partially saturated Berea sandstone: Evidence of fluid flow on the mesoscopic scale. *Geophysical Journal International*, *195*, 342–351. https://doi.org/10.1093/gji/ggt259

Toms-Stewart, J., Müller, T. M., Gurevich, B., & Paterson, L. (2009). Statistical characterization of gas-patch distributions in partially saturated rocks. *Geophysics*, *72*(2), WA51–WA64.

Tronicke, J., & Holliger, K. (2005). Quantitative integration of hydrogeophysical data: Conditional geostatistical simulation for characterizing heterogeneous alluvial aquifers. *Geophysics*, *70*, H1–H10. https://doi.org/10.1190/1.1925744

White, J. E. (1975). Computed seismic speeds and attenuation in rocks with partial gas saturation. *Geophysics*, *40*, 224–232. https://doi.org/10.1190/1.1440520

White, J. E., Mikhaylova, N. G., & Lyakhovitskiy, F. M. (1975). Low-frequancy seismic waves in fluid-saturated layered rocks. *Physics Solid Earth*, *11*, 654–659. https://doi.org/10.1121/1.1995164

Winkler, K., & Nur, A. (1979). Pore fluids and seismic attenuation in rocks. *Geophysical Research Letters*, *6*(1), 1–4.

Wood, A. (1955). *A textbook of sound*. New York: MacMillan Publishing Company.

Yin, C. S., Batzle, M. L., & Smith, B. J. (1992). Effects of partial liquid/gas saturation on extensional wave attenuation in Berea sandstone. *Geophysical Research Letters*, *19*(13), 1399–1402.

Zhang, Y., Nishizawa, O., Kiyama, T., & Xue, Z. (2015). Saturation-path dependency of *P*-wave velocity and attenuation in sandstone saturated with CO_2 and brine revealed by simultaneous measurements of waveforms and X-ray computed tomography images. *Geophysics*, *80*, D403–D415. https://doi.org/10.1190/GEO2014-0289.1